PHYSICAL REVIEW B **77**, 184406 (2008)

Local structure in magnetostrictive melt-spun $Fe_{80}Ga_{20}$ alloys

S. Pascarelli,[1] M. P. Ruffoni,[1] R. Sato Turtelli,[2] F. Kubel,[3] and R. Grössinger[2]
[1]*European Synchrotron Radiation Facility, Boîte Postale 220, 38043 Grenoble Cedex, France*
[2]*Institute of Solid State Physics, Vienna University of Technology, A-1040 Vienna, Austria*
[3]*Department of Chemical Technologies and Analytics, Vienna University of Technology, A-1060 Vienna, Austria*

(Received 10 December 2007; revised manuscript received 9 April 2008; published 5 May 2008)

We perform a detailed investigation of the local atomic structure in highly magnetostrictive α-FeGa melt-spun ribbons. By using extended x-ray absorption fine structure (EXAFS) analysis at the Fe and Ga K edges coupled to x-ray diffraction (XRD) and to *ab initio* full multiple scattering calculations of the x-ray absorption near edge structure (XANES), we test for the presence of different local defect structures proposed in literature as being responsible for the large magnetostriction in these alloys. XRD shows that the ribbons crystallize in the A2 phase. Invisible by XRD, the presence of small Ga clusters is excluded by both EXAFS and XANES since no first shell Ga-Ga bonds are detected. However, EXAFS analysis of the second coordination shell around Ga clearly provides evidence for the presence of one highly strained (+4%) Ga-Ga pair and five Ga-Fe pairs, among the six crystallographically equivalent $\langle 001 \rangle$ atomic pairs. This conclusion supports recent total energy calculations that assign the large magnetostriction in these alloys to the strain caused by the rotation of the magnetization in the vicinity of such defects.

DOI: 10.1103/PhysRevB.77.184406 PACS number(s): 75.50.Bb, 75.80.+q

I. INTRODUCTION

The study of magnetostriction began in 1842 when James Joule first observed that a sample of iron changes its length when magnetized. The term itself refers to any change in the dimensions of a magnetic material caused by a change in its magnetization and has its origin in spin-orbit coupling, wherein such materials convert (or transduce) magnetic energy into mechanical energy and vice versa. Magnetostricton is an inherent material property that will not degrade with time. With the discovery of "giant" magnetostrictive alloys in the 1970s,[1] there has been a renewed interest in magnetostrictive transducer technologies. Many uses for magnetostrictive actuators, sensors, and dampers have surfaced in the last two decades as more reliable and larger strain and force giant magnetostrictive materials such as Terfenol-D (Ref. 2) have become commercially available.

In recent years, Fe based metallic alloys have been the subject of considerable interest for magnetostrictive applications. In its pure, elemental form, Fe is well known to possess a very small magnetostriction. However, initial experiments performed on FeAl alloys,[3] and subsequently on FeGa alloys,[4] revealed that when an additional metallic element is dissolved into the Fe lattice, an enhancement in magnetostriction of somewhere between one and two orders of magnitude can be observed. Consequently, these alloys, and particularly $Fe_{(1-x)}Ga_x$ based alloys, have attracted significant interest from a technological and device applications perspective since, although they have not been shown to truly possess giant magnetostrictions (unlike, say, the much studied Terfenol-D), they both lack expensive rare-earth components and possess much more desirable mechanical properties. They also show appreciable low-field magnetostriction, with saturation fields of only several hundred Oersteds. For high power transducer applications, high strain at low fields is necessary. Therefore, a low anisotropy is important to maximize domain wall mobility and permit domain rotation at low fields. Usually, magnetostriction is accompanied by a large anisotropy, whereas, $Fe_{(1-x)}Ga_x$ based alloys at specific composition x are characterized by a very low magnetic anisotropy. A recent review of the development of the Fe-Ga (also called Galfenol) system for magnetostriction applications can be found in Ref. 5.

From very early on, it was appreciated that the magnetostriction exhibited by a particular $Fe_{(1-x)}Ga_x$ sample relied not just on the relative Ga concentration in the solid solution but also very heavily on the sample preparation technique and its subsequent thermal history since these combine to produce different crystallographic textures and grain morphologies.[6–10] In rapidly quenched samples, structural analyses indicate that a disordered A2 phase may be retained up to about 20 at. % Ga, whereas at higher concentrations or with other preparation techniques, ordered $D0_3$ and tetragonal B2-like phases emerge.[6,11] In each case, the fraction of sample possessing each structure plays an important role in determining what degree of enhanced magnetostriction is observed.

Initially, Clark *et al.*[6] proposed that such enhancements are due to the clustering of the solute atoms in the disordered A2 phase (also commonly cited as α-FeGa) to provide both elastic and magnetoelastic defects, which decrease in number as the concentration of solute increase and $D0_3$ and B2 phases emerge. However, in 2002, Wu[12] performed *ab initio* calculations that suggested that it is in fact the tetragonal B2-like phase that produces the large positive magnetostriction macroscopically observed. This was more recently developed by Cullen *et al.*,[13] who identified $\langle 001 \rangle$ Ga-Ga pairs as responsible for the high magnetostriction in α-FeGa. Cullen *et al.*[13] also showed that the low magnetic anisotropy typical of $Fe_{(1-x)}Ga_x$ with $x \sim 0.2$ can be explained by a competition between a coherent anisotropy energy (due to the Fe host lattice) and a randomly oriented local anisotropy (due to the random distribution of Ga-Ga pairs along the $\langle 001 \rangle$ direction), which leads to very small net anisotropy.

It is therefore clear that in order to gain an experimental understanding of the fundamental magnetostrictive behavior of $Fe_{(1-x)}Ga_x$ and assess the validity of such theoretical models, the first step must be to determine a sample's local atomic structure. To date, however, structural analyses of $Fe_{(1-x)}Ga_x$ have focused on macroscopic or long-range order techniques such as transmission electron microscopy or x-ray diffraction (XRD). Here, though, we present a structural analysis of a melt-spun ribbon of $Fe_{80}Ga_{20}$ performed with x-ray absorption spectroscopy (XAS) in conjunction with standard XRD. This provides the required local structural information, which is typically limited to the first one or two atomic shells surrounding an absorbing atom. It also provides chemical selectivity, which allows the structure to be assessed from both the perspectives of the Fe atoms and of the Ga atoms, which in turn allows information to be obtained on the specific types of bond: Fe-Fe, Fe-Ga, and Ga-Ga.

The paper is organized as follows. Section II reports information on the sample preparation and laboratory characterization, as well as on experimental details of the XRD and XAS measurements. Section III is dedicated to the experimental data and analysis procedures: In Sec. III A, we report the XRD data, as well as the results of the Rietveld refinement of the XRD patterns; in Sec. III B, we report the XAS data and in detail describe the analysis procedures that are different for the extended x-ray absorption fine structure (EXAFS) region (Sec. III B 1) and for the x-ray absorption near edge structure (XANES) region (Sec. III B 2). Section IV reports the results obtained from the analysis of the XAS data. We discuss our findings in the light of recent theoretical calculations. Finally, Sec. V gives the main conclusions of this work.

II. EXPERIMENT

The $Fe_{80}Ga_{20}$ alloy was prepared by arcmelting. Iron and gallium of high purity (>99.9%) were melted together by using an induction furnace under an argon atmosphere. The furnace power was increased and diminished three times during each melting step in order to assure homogeneity. The melt was solidified by ejection onto a water-cooled rotating copper wheel to produce a rapidly quenched ribbon sample with a thickness of 60 μm and a width of 3 mm. The best ribbons (thicker and wider) were obtained from a nozzle of a diameter between 0.75 and 0.80 mm, a distance from the nozzle to the copper disk of 2 mm, and a copper disk velocity of 10 m/s. The concentrations of Fe and Ga in this as-quenched ribbon were determined by means of energy dispersive x-ray analysis spectrometry (ISIS 300 of Oxford Instruments coupled to a scanning electron microscope, LEO model 1450VP). The measured compositions were $c_{Fe} = 80.0 \pm 0.5$ and $c_{Ga} = 20.0 \pm 0.5$. The microstructure exhibited columnar grains in the solidification direction, as illustrated by the optical micrograph shown in Fig. 1. The ribbon itself was ductile (that is, full bending was possible) and exhibited a large magnetostriction of about 700 ppm in the direction of the thickness of the ribbon, which was measured by using a miniature capacitance dilatometer under an applied field along the ribbon axis[10] with almost no hysteresis in the magnetostriction vs applied field curve.

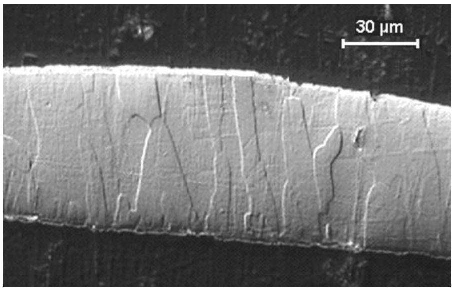

FIG. 1. Optical micrograph of the as-quenched ribbon. The microstructure exhibits columnar grains in the solidification direction.

X-ray diffraction was measured from both ribbon sides, the quenched side (wheel) and the unquenched side (free), on several $Fe_{80}Ga_{20}$ ribbon samples in two different geometries: (1) fixed sample (beam parallel to the ribbon) and (2) rotating sample holder. The powder XRD patterns were recorded by means of an Xpert Philips powder diffractometer (Goniometer Philips PW 3050/60) using $CuKa_{1,2}$ radiation in a Bragg Brentano geometry and an X'Celerator detector. The x-ray generator Philips PW 3040/60 worked at a power of 40 kV and 40 mA, and the goniometer was equipped with a graphite monochromator. Diffraction patterns were recorded in the angular range of $5°-135°$ with a scan step size of 0.02°. Collected data were refined by using the Rietveld package TOPAS (BRUKER AXS TOPAS V 2.1) based on the fundamental parameter approach, with the diffractometer parameters and wavelength settings adjusted by using a LaB_6 standard.

XAS measurements were performed on a 7 mm thick sample, which was obtained by polishing both the wheel and the free sides of the ribbon. Fe and Ga *K* edge EXAFS were recorded in the transmission mode at beamline BM29 of the European Synchrotron Radiation Facility[14] (ESRF) by using a double crystal fixed exit Si(111) monochromator and a pair of Si mirrors for harmonic rejection. A 4 μm thick high purity Fe foil (Goodfellow) was used as a standard.

III. DATA ANALYSIS

A. X-ray diffraction

The XRD patterns obtained in the two geometries were found to differ only by background intensities, so we report here the results from one of the rotating samples. The refined patterns show no deviation from the A2 phase and no supplementary reflections were observed. The background function was refined by using a Chebychev polynomial. The refinements converged at R_{Bragg} values of 0.41% and 0.25%, respectively (the low values are related to the background intensity). For the wheel (free) side, the global agreement factors were R_{exp}: 1.18 (1.16); R_{wp}: 1.81 (1.77); R_p: 1.31 (1.27); and GOF: 1.54 (1.53), which confirm the models. Vibrational parameters B_{eq} of 0.2 were assumed. Refinements on different lattice systems did not improve the model.

The lattice constants of 2.90604(3) and 2.905423(21) Å were found, respectively, for the wheel and free sides. The

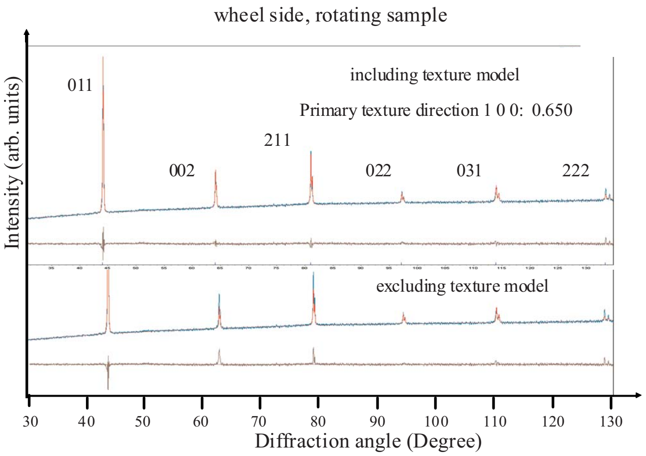

FIG. 2. (Color online) Refined XRD patterns obtained on the wheel side of the ribbon with (top) and without (bottom) applying a textured model in the refinement: data (blue line), calculation (red line), and difference (gray line).

refined values agree with the 2.907 Å given in literature.[15] The crystallite size was determined based on a Lorentzian size refinement following the Scherrer[16] approach. The wheel and free sides of the ribbons where characterized by different average crystallite sizes: $D=159\pm3$ nm and $D=262\pm8$ nm, respectively. As expected, fast cooling gives rise to a smaller crystallite size.

In all refinements, a pronounced texture model was used to obtain reasonable fits. For both ribbon sides, observed, refined, and difference patterns are given in Figs. 2 and 3, respectively, with and without applying a texture model. It can be seen that the two sides differ in texture. The wheel side shows mainly a primary (100) texture, refining to $P=0.650\pm0.002$ ($P=1$: untextured and $P=0$: fully textured sample) and a minor (211) texture, whereas the free side is affected by a stronger (100) texture (refining to $P=0.478\pm0.001$), in addition to weak (211) and (031) texture contributions.

The presence of texture effects on both sides is rather surprising but could be related to a mechanical compression on the copper wheel. This explanation would also be compatible with the lower degree of texture on the quenched side.

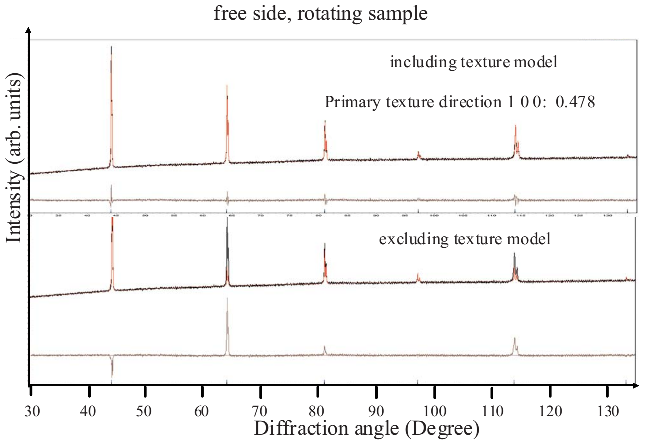

FIG. 3. (Color online) Refined XRD patterns obtained on the free side of the ribbon with (top) and without (bottom) applying a textured model in the refinement: data (black line), calculation (red line), and difference (gray line).

B. X-ray absorption spectroscopy

X-ray absorption spectroscopy is particularly suited to probe the local environment of an absorber atom in condensed matter. An x-ray absorption spectrum can be roughly divided into two regions that cannot be described by using the same theoretical approximations: the energy region close to the absorption, or the XANES region, and the region that extends up to ~1000 eV or more above the absorption edge, the so-called EXAFS region. EXAFS refers to the oscillatory structure in the x-ray absorption coefficient. It is a unique signature of a given atom embedded in a given system and depends on the local atomic structure and vibrational properties of the material.[17]

The EXAFS region, which is characterized by a relatively large photoelectron energy (>50 eV) with a relatively low mean free path, can be interpreted in a simplified manner by using a single-scattering formalism, whereby the emitted photoelectron wave is scattered once by the electronic potentials of the neighboring atoms. The XANES region on the other hand, where the photoelectron energy is low and its mean free path is large, arises from complex multiple scattering processes and its interpretation is difficult: First, because a single scattering formalism is totally unable to describe it and second, because details in the description of the potentials cannot be so easily neglected as can be done in the EXAFS region.

EXAFS is very sensitive to the first neighbor shells and can yield information on the chemical nature of the nearest neighbors, their number, their distance from the absorber atom, and their thermal and static disorders relative to the absorber atom. XANES, on the other hand, is very sensitive to the local bonding geometry and electronic structure.

We independently analyzed the EXAFS and the XANES regions. A quantitative analysis of the EXAFS region is given in Sec. III B 1 by using well established standard procedures. The XANES region, on the other hand, has allowed us to confirm our EXAFS conclusions by a qualitative comparison between the data and *ab initio* simulations since the quantitative analysis of absorption spectra close to the edge remains still very challenging up until now. This is described in Sec. III B 2.

1. Quantitative analysis of EXAFS region

The EXAFS data analysis was performed by using the codes from the UWXAFS package.[18] The experimental XAFS functions $\chi(k)$ were obtained after subtracting the embedded-atom absorption background from the measured absorption coefficient and normalizing by the edge step using the program AUTOBK.[19] As a starting point for our EXAFS analysis, we built a structural model based on our x-ray diffraction results, i.e., the A2 phase with lattice parameter 2.90 Å.

Ab initio scattering phases and amplitudes for photoabsorber (Fe and Ga) and backscatterer (Fe and Ga) atoms were calculated by FEFF8 (Ref. 20) by using a self-consistent en-

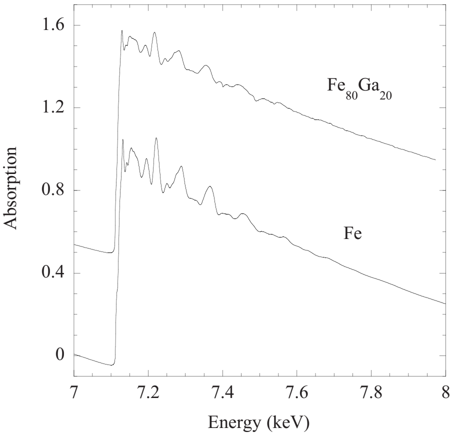

FIG. 4. EXAFS Fe *K* edge spectra obtained on the $Fe_{80}Ga_{20}$ ribbon and pure Fe foil.

ergy dependent exchange correlation Hedin–Lundqvist potential. The ATOMS program[21] was used to build the atomic clusters, which are centered on Fe or on Ga, and to prepare the input for FEFF8.

In this work, we limited our EXAFS analysis to the region of R space that extends up to about 3 Å from the absorber, i.e., the first two coordination shells of the A2 lattice. The only paths contributing to the EXAFS signal in this R range are two single scattering paths corresponding to the first and second shell.

Figures 4 and 5 show the EXAFS spectra obtained on the FeGa ribbon at the Fe and Ga K edges, respectively. The Fe foil standard is also shown in Fig. 4. The extracted EXAFS oscillations $\chi(k)$, which are plotted as a function of photoelectron wave-vector k, are shown in Fig. 6.

A qualitative picture of the local structure around Fe and around Ga can be obtained from the Fourier transforms (FT) of the EXAFS signals (Fig. 7). The FT has been performed in the range $2.6 \leq k \leq 15.0$ Å^{-1}. At first sight, the FTs look very similar, which suggests that the local geometry around the absorber, be it Fe or Ga, is very similar to that in pure bcc Fe (shown in the top curve of Fig. 7). The first peak centered at around 2.2 Å corresponds, once phase shifts are accounted for, to the interaction between the absorber atom and the first two neighboring shells of the bcc lattice at around 2.5 and 2.9 Å. The closeness of these two neighboring shells combined with the effect of static and thermal disorder and the limited R-space resolution does not allow us to resolve these two shells by eye, but is possible in the fitting procedure.

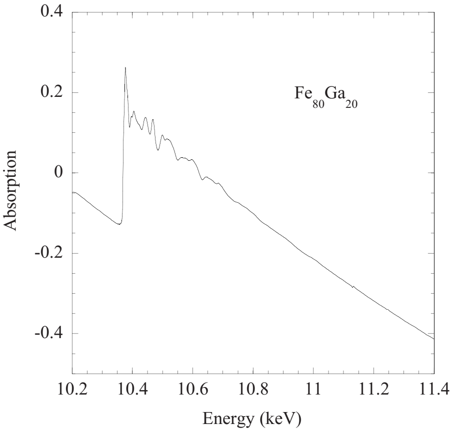

FIG. 5. EXAFS Ga *K* edge spectrum obtained on the $Fe_{80}Ga_{20}$ ribbon.

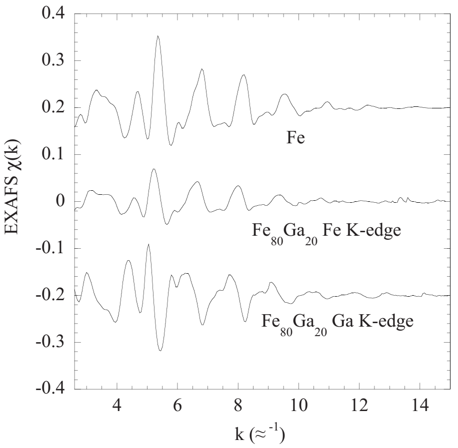

FIG. 6. Extracted normalized EXAFS oscillations $\chi(k)$ plotted as a function of photoelectron wave-vector k. Top: pure Fe foil; middle: Fe *K* edge on $Fe_{80}Ga_{20}$; and bottom: Ga *K* edge on $Fe_{80}Ga_{20}$.

In order to extract the local structural parameters—bond distances, R, relative mean square displacements (msrd), $\Delta\sigma^2$, and the ratio between Ga/Fe scatterers (x)—we performed a least square fitting of this first peak of the FT in the region $1.0 \leq R \leq 3.0$ Å by using the program FEFFIT.[22] We constructed a model EXAFS signal $\chi^{\text{model}}(k)$ as the sum of the first and second shell single scattering paths with variable fitting parameters for energy offsets, bond distances, and msrds for the two shells. Total coordination numbers were fixed to nominal values in the bcc lattice: eight atoms in the first shell and six atoms in the second shell.

For the Fe K edge model, the Fe-Fe interatomic distances of the first R^{I} and second shell R^{II} were linked by crystallographic constraints: $R^{\text{II}} = (2/\sqrt{3})R^{\text{I}}$. The chemical composition of the first shell around Fe was left as a variable fitting

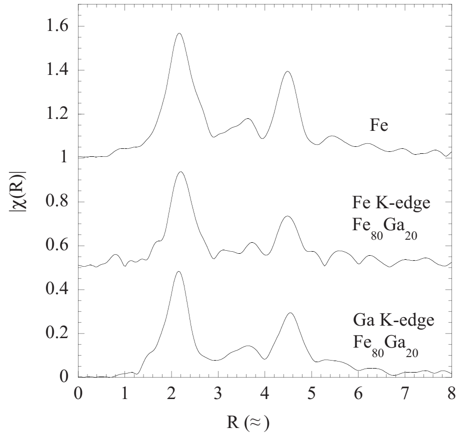

FIG. 7. Amplitudes of the Fourier transforms of the EXAFS $\chi(k)$ signals $|\chi(R)|$. Top: pure Fe foil; middle: Fe *K* edge on $Fe_{80}Ga_{20}$; bottom: Ga *K* edge on $Fe_{80}Ga_{20}$.

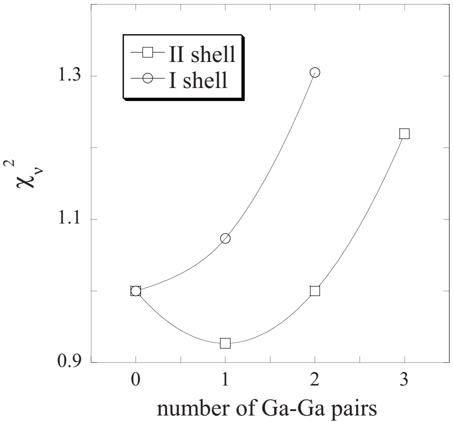

FIG. 8. Reduced χ^2 values, χ_v^2, obtained for the simultaneous Ga K edge and Fe K edge fits of the $Fe_{80}Ga_{20}$ data with different structural models for the first and second shells around Ga. χ_v^2 values are normalized to the value obtained for a fit with no Ga atoms in the first or second shell.

parameter. The presence of Ga atoms in the second shell around Fe was tested.

For the Ga K edge model, the Ga-Fe interatomic distances of the first and second shell were left as variable fitting parameters, to account for lattice relaxation that is expected to be more important for the first shell.[23] The presence of Ga in the first and second shell was tested by progressively substituting one Fe atom with one Ga atom.

The Fe and Ga K edge data for the same sample were simultaneously fitted. The fitting parameters were, for each edge (the superscripts I and II refer to first and second shell fitting parameters, respectively): (1) E_0 offset: $E_{0-\mathrm{Fe}}$ and $E_{0-\mathrm{Ga}}$; (2) average relative atomic displacements with respect to crystallographic distances $\alpha=\Delta R/R$: $\alpha^{\mathrm{I}}_{\mathrm{FeFe}}=\alpha^{\mathrm{II}}_{\mathrm{FeFe}}$ for the Fe-Fe atomic pairs, $\alpha^{\mathrm{I}}_{\mathrm{GaFe}}=\alpha^{\mathrm{I}}_{\mathrm{FeGa}}$ and $\alpha^{\mathrm{II}}_{\mathrm{GaFe}}$ for the Fe-Ga atomic pairs and $\alpha^{\mathrm{I}}_{\mathrm{GaGa}}$ and $\alpha^{\mathrm{II}}_{\mathrm{GaGa}}$ for the Ga-Ga pairs; (3) chemical composition of first shell around Fe, $x=\mathrm{N}_{\mathrm{FeGa}}/(\mathrm{N}_{\mathrm{FeGa}}+\mathrm{N}_{\mathrm{FeFe}})$; (4) msrd for the Fe-Fe atomic pairs $(\Delta\sigma^2)^{\mathrm{I}}_{\mathrm{FeFe}}$ and $(\Delta\sigma^2)^{\mathrm{II}}_{\mathrm{FeFe}}$, msrd for the Fe-Ga atomic pairs $(\Delta\sigma^2)^{\mathrm{I}}_{\mathrm{GaFe}}=(\Delta\sigma^2)^{\mathrm{II}}_{\mathrm{FeGa}}$ and $(\Delta\sigma^2)^{\mathrm{II}}_{\mathrm{GaFe}}$, and msrd for the Ga-Ga atomic pairs $(\Delta\sigma^2)^{\mathrm{I}}_{\mathrm{GaGa}}$ and $(\Delta\sigma^2)^{\mathrm{II}}_{\mathrm{GaGa}}$. The amplitude factor S_0^2 was fixed to 0.9.

The fitting was performed on Fourier filtered $\chi(k)$ data $\chi(q)$ in the range $2.6 \leq q \leq 15.0$ Å^{-1}. The suitability of each model was evaluated by comparing reduced χ^2 variables χ_v^2 i.e., the χ^2 variable divided by the number of degrees of freedom in the fit: $\nu=N_{\mathrm{idp}}-N_{\mathrm{var}}$, where N_{idp} and N_{var} are the numbers of independent measurements in a spectrum and the number of variables in the fit, respectively.

At the Fe K edge, adding a second shell Fe-Ga contribution, with $R^{\mathrm{II}}_{\mathrm{Fe\text{-}Ga}}$ and $(\Delta\sigma^2)^{\mathrm{II}}_{\mathrm{FeGa}}$ equal to Ga K edge values, did not change the χ_v^2 of the fit, which indicates that we do not have the sensitivity to determine the presence of Ga in the second shell around Fe. At the Ga K edge, we tested for the presence of Ga-Ga first shell and second shell interactions. Figure 8 shows the χ_v^2 values corresponding to fits wherein one first shell Ga-Fe pair (empty circles) was progressively substituted with one Ga-Ga pair and wherein one second shell Ga-Fe pair (empty square) was progressively substituted with one Ga-Ga pair. This shows that, whereas any addition of Ga in the first shell yields a statistically less valid model, the introduction of one second shell Ga-Ga pair immediately leads to a reduction of χ_v^2 of ~10%. Further addition of Ga-Ga pairs rapidly decreases the quality of the fit.

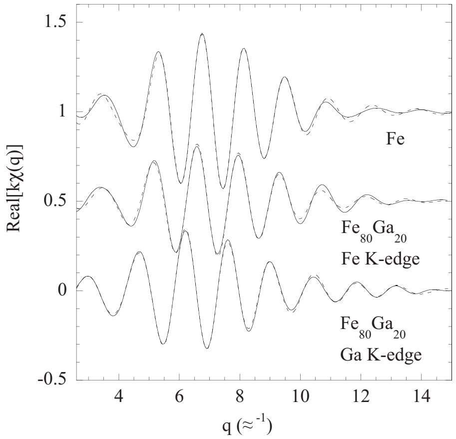

FIG. 9. Comparison between the real part of the Fourier filtered $\chi(k)$, real $[\chi(q)]$ (solid line), and best fits (dashed line) at the Fe and Ga K edges in q space. Top: pure Fe foil; middle: Fe K edge on $Fe_{80}Ga_{20}$; and bottom: Ga K edge on $Fe_{80}Ga_{20}$.

Figures 9 and 10 show the results of the best fits at the Fe and Ga K edges in q and R space, respectively, whereas Tables I and II report the results for the best fit parameters at the Fe and Ga K edges, respectively (Fe-Ga first shell parameters were set equal at the two edges and are shown only in Table II).

2. Qualitative Analysis of XANES region

We used the FEFF8.2 (Ref. 19) code to perform full multiple scattering calculations to simulate the XANES region of the spectra at the Fe and Ga K edges. *Ab initio* scattering amplitudes and phases were calculated by using a complex Hedin–Lundvquist potential, with the electronic density self-

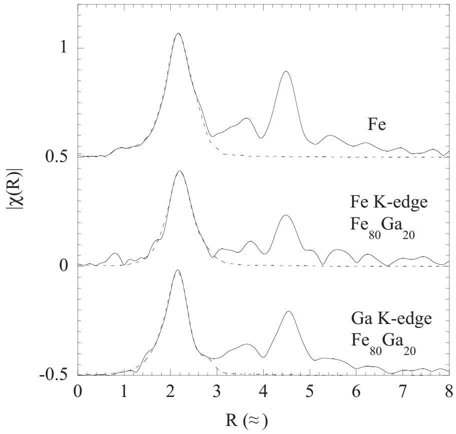

FIG. 10. Amplitudes of the Fourier transforms of the EXAFS $\chi(k)$ signals, $|\chi(R)|$ (solid line), and best fits (dashed line) at the Fe and Ga K edges in R space. Top: pure Fe foil; middle: Fe K edge on $Fe_{80}Ga_{20}$; and bottom: Ga K edge on $Fe_{80}Ga_{20}$.

TABLE I. Fe K edge best fit structural parameters. The first shell Fe-Ga distance and mean square relative displacement are set equal for both edges and are shown only in Table II.

	First shell Ga content x	$R^{\mathrm{I}}_{\mathrm{FeFe}}$ (Å)	$R^{\mathrm{II}}_{\mathrm{FeFe}}$ (Å)	$(\Delta\sigma^2)^{\mathrm{I}}_{\mathrm{FeFe}}$ 10^{-3} (Å^2)	$(\Delta\sigma^2)^{\mathrm{II}}_{\mathrm{FeFe}}$ 10^{-3} (Å^2)	E_0 (eV)
Fe		2.465(7)	2.846(8)	6.6(5)	6.0(9)	1(1)
$Fe_{80}Ga_{20}$	0.3(1)	2.50(1)	2.89(2)	7(1)	11(3)	0(2)

consistently calculated within a radius of 5.5 Å from the absorber. All scattering paths within the same atomic cluster (approximately 60 atoms) were summed to infinite order.

The imaginary part of the potential was not optimized and our simulations underestimate this damping at the absorption edge. Moreover, no disorder factor was introduced in the calculations, so that the high energy fine structure is also underdamped in the simulations, compared to the experimental data.

Figure 11 reports the simulations for Fe K edge XANES in (i) the pure Fe bcc phase (a=2.87 Å), (ii) the $Fe_{80}Ga_{20}$ A2 phase (a=2.90 Å), wherein 12 Fe atoms out of 59 (about 20%) have been substituted by Ga, and (iii) the $D0_3$ Fe_3Ga phase (a=2.90 Å), wherein the first and second shell are composed of eight Fe and six Ga atoms, respectively.

Figure 12 compares the experimental data at the Fe K edge between pure Fe foil and the $Fe_{80}Ga_{20}$ ribbon sample. We can see that in the experimental data, the main effects of adding Ga to bcc Fe are a less pronounced bump at the onset of absorption, a damped white line, and a slight shift to lower energies of the oscillations, including the white line position. A qualitative comparison between Figs. 11 and 12 indicates that all of the observed features are reproduced by the A2 model, which is in agreement with our XRD and EXAFS results.

Figure 13 reports the Ga K edge simulations. The topmost spectrum corresponds to the $D0_3$ phase (a=2.90 Å), wherein the first and second shells are composed of eight and six atoms of Fe, respectively. All of the other curves are relative to the A2 phase with different atomic distributions. Shown from bottom to top are (a) Ga surrounded only by Fe atoms; (b) Ga surrounded by a first shell composed of eight Fe atoms and a second shell composed of one Ga atom and five Fe atoms, with further shells being only Fe; (c) Ga surrounded by a first shell composed of one Ga atom and seven Fe atoms, with further shells being only Fe; (d) Ga surrounded only by Ga in the first shell and by Fe in further shells; and (e) 20% Ga atoms randomly distributed in all of the shells.

The experimental XANES Ga K edge is shown in Fig. 14. The inset reports simulations (a)–(c), which are the only ones able to reproduce the shape of the white line. However, simulation (a) features a very pronounced bump at the onset of absorption that is less evident on the data. Both simulations (b) and (c) reproduce all of the features of the experimental data, although the shape of the white line is slightly closer to (b).

IV. RESULTS AND DISCUSSION

The quantitative EXAFS results reported in Fig. 8 and Tables I and II, and the qualitative XANES results shown in Figs. 13 and 14, are consistent with the following picture of the local structure around Fe and Ga in melt-spun ribbons of $Fe_{80}Ga_{20}$:

The first evident result is that Ga clustering does not occur in our ribbon. The presence of small Ga clusters, which are undetectable by XRD, was proposed as a possible origin of strain in the highly magnetostrictive α-FeGa alloys.[3] From a local structure point of view, such clusters would manifest themselves as Ga surrounded by a first shell predominantly composed of Ga atoms. EXAFS analysis at the Ga K edge shows that even one Ga-Ga first shell bond is unlikely to occur (see Fig. 8). XANES simulations show that a first shell composed of eight Ga atoms yields a white line shape, which is shown in simulation (d) in Fig. 13, which is not compatible with the data.

The distribution of Ga around Fe can be described by a close to random distribution, with perhaps a slight tendency to cluster around Fe. EXAFS analysis, in fact, shows that the Ga content in the first shell around Fe (Table I) is on the order of 0.3 (1), which is slightly higher than that expected for a perfectly random distribution (0.2). The evolution of the Fe K edge XANES simulations when Ga is randomly added to the bcc Fe lattice (Fig. 11) is compatible with the evolution of the experimental data shown in Fig. 12.

The distribution of Ga around Ga shows interesting features: Whereas, no Ga is present in the first shell, one Ga atom is very likely to be present in the second coordination shell, as illustrated in Fig. 8. XANES analysis also supports this finding (Fig. 14). The detection of Ga-Ga second shell interactions supports the hypothesis by which the large magnetostriction and the low magnetic anisotropy typical of α-FeGa alloys are to be attributed to randomly arranged

TABLE II. Ga K edge best fit structural parameters. The first shell Ga-Fe distance and mean square relative displacement are set equal for both edges and are shown only in Table II.

$R^{\mathrm{I}}_{\mathrm{GaFe}}$ (Å)	$R^{\mathrm{II}}_{\mathrm{GaFe}}$ (Å)	$R^{\mathrm{II}}_{\mathrm{GaGa}}$ (Å)	$(\Delta\sigma^2)^{\mathrm{I}}_{\mathrm{GaFe}}$ 10^{-3} (Å^2)	$(\Delta\sigma^2)^{\mathrm{II}}_{\mathrm{GaFe}}$ 10^{-3} (Å^2)	$(\Delta\sigma^2)^{\mathrm{II}}_{\mathrm{GaGa}}$ 10^{-3} (Å^2)	E_0 (eV)
2.526(4)	2.877(6)	3.00(2)	6.7(3)	10(1)	3(2)	−1.8(7)

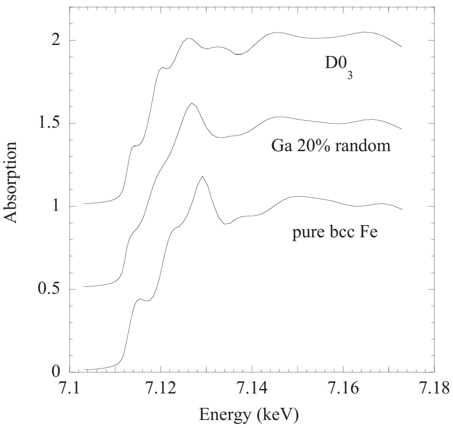

FIG. 11. FEFF8.2 full multiple scattering simulations of the Fe *K* edge XANES. Top: $D0_3$ phase; middle: A2 phase with 20% Ga randomly distributed; and bottom: pure bcc Fe.

⟨001⟩ strained Ga-Ga pairs, which act as local defects.[13]

The substitution of Fe by Ga introduces important local strain. First shell Fe-Ga bonds exhibit a +1% strain with respect to first shell Fe-Fe bonds. This strain rapidly relaxes down to below 0.5% on second Fe-Ga shell bonds. On the other hand, the interatomic second shell Ga-Ga distance (3.00 ± 0.02 Å) is highly strained ($\sim +4\%$) with respect to the corresponding Fe-Fe distance of the host lattice (2.89 ± 0.02 Å).

Such an important local strain around the randomly distributed Ga-Ga pairs is evidently responsible for the interesting magnetostrictive behavior of the α-FeGa system at these compositions. Here, we also found a possible explanation for the absence of first shell Ga-Ga bonds, which can be seen as a mechanism for the distorted crystal to minimize the elastic energy since the expected strain on such hypothetical bonds would probably be close to ~10%.

Substitutional pairs in a bcc crystal can have orthorhombic ⟨110⟩ pair, tetragonal, ⟨001⟩ pair, or trigonal ⟨111⟩ pair symmetries. Detection of ⟨001⟩ Ga-Ga pairs in α-FeGa is in full agreement with anelastic data on the anisotropy of the internal friction in bcc alloys.[24]

From a microscopic point of view, the existence of ⟨001⟩ Ga pairs produces a tendency for the spin in the neighboring Fe lattice to align parallel or perpendicular to the Ga-Ga pair. This effect modifies the total energy of the system by introducing a randomly directed local uniaxial anisotropy energy that accounts for the effect the Ga-Ga pairs have on the neighboring Fe moments. Reference 13 shows how this model gives a plausible explanation both for the reduction and eventual collapse of the anisotropy and for the large magnetostrictive strain in α-FeGa. In terms of this model, the magnetostriction would be interpreted as the average strain that is induced by the randomly arranged ⟨001⟩ defects.

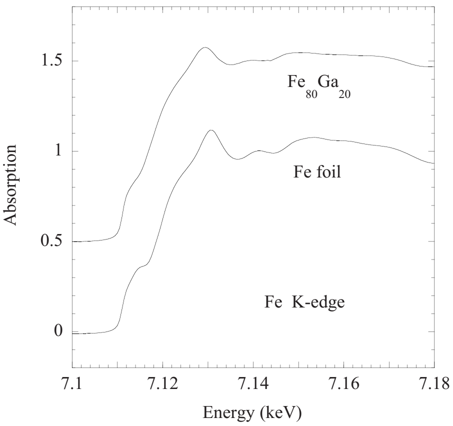

FIG. 12. Fe *K* edge XANES experimental data. Top: Fe *K* edge on $Fe_{80}Ga_{20}$ and bottom: pure Fe foil.

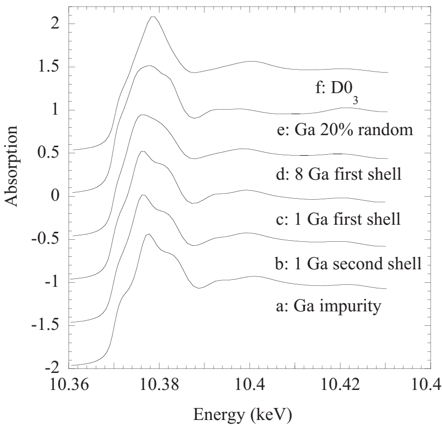

FIG. 13. FEFF8.2 full multiple scattering simulations of the Ga *K* edge XANES. From bottom to top: (a) Ga surrounded only by Fe atoms; (b) Ga surrounded by a first shell composed only of Fe atoms and a second shell composed of one Ga atom and five Fe atoms; (c) Ga surrounded by a first shell composed of one Ga atom and seven Fe atoms; (d) Ga surrounded only by Ga in the first shell and by Fe in further shells; (e) 20% Ga atoms randomly distributed in all of the shells; and (f) the $D0_3$ phase.

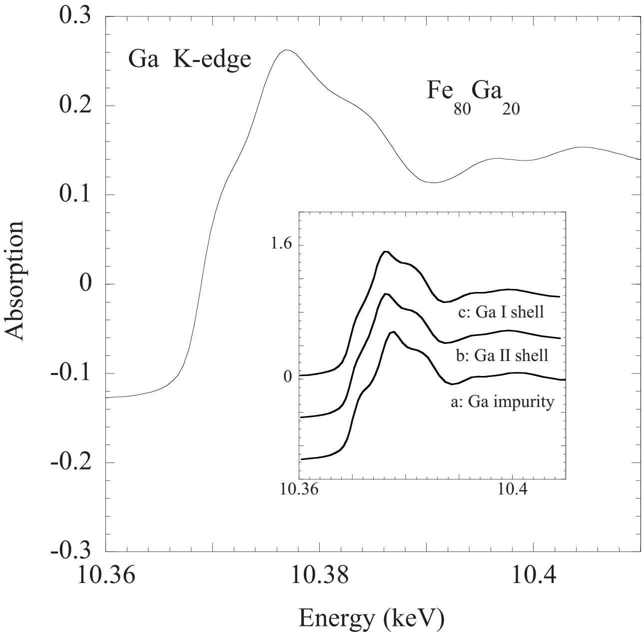

FIG. 14. Ga *K* edge XANES experimental data on $Fe_{80}Ga_{20}$. The inset shows simulations (a)–(c) from Fig. 13.

V. CONCLUSION

We provide, for the first time, a detailed description of the local atomic structure in the highly magnetostrictive α-FeGa melt-spun ribbons by using chemically selective and local atomic probes such as EXAFS and XANES spectroscopies coupled to XRD. We test for the presence of different local defect structures proposed in literature as being responsible for the large magnetostriction in these alloys. We find that $Fe_{80}Ga_{20}$ melt-spun ribbons crystallize in the A2 phase (chemically disordered bcc lattice) and that Ga atoms almost randomly substitute Fe sites, introducing local strain. We provide evidence for the existence of local defects that introduce important strains on the order of $\sim+4\%$ in the form of second shell Ga-Ga pairs, which in the bcc lattice are oriented in the $\langle 001\rangle$ crystallographic direction. The detection of Ga-Ga second shell interactions supports the recent hypothesis by which the large magnetostriction and the low magnetic anisotropy typical of α-FeGa alloys are to be attributed to randomly distributed $\langle 001\rangle$ strained Ga-Ga pairs. The rotation of the magnetization in the vicinity of the defect could therefore be at the origin of the interesting magnetostrictive behavior of α-FeGa for compositions close to 20%.

ACKNOWLEDGMENTS

We thank the technicians of BM29 Sebastien Pasternak and Florian Perrin for assistance during the experiment.

[1] A. E. Clark and H. S. Belson, Phys. Rev. B **5**, 3642 (1972).

[2] A. E. Clark and D. N. Crowder, IEEE Trans. Magn. **21**, 1945 (1985).

[3] R. C. Hall, J. Appl. Phys. **28**, 707 (1957).

[4] A. E. Clark, J. B. Restorff, M. Wun-Fogle, T. A. Lograsso, and D. L. Schlagel, IEEE Trans. Magn. **36**, 3238 (2000).

[5] E. M. Summers, T. A. Lograsso, and M. Wun-Fogle, J. Mater. Sci. **42**, 9582 (2007).

[6] A. E. Clark, M. Wun-Fogle, J. B. Restorff, T. A. Lograsso, and J. R. Cullen, IEEE Trans. Magn. **37**, 2678 (2001).

[7] S. F. Cheng, B. N. Das, M. Wun-Fogle, P. Lubitz, and A. E. Clark, IEEE Trans. Magn. **38**, 2838 (2002).

[8] R. A. Kellogg, A. B. Flatau, A. E. Clark, M. Wun-Fogle, and T. A. Lograsso, J. Appl. Phys. **93**, 8495 (2003).

[9] T. A. Lograsso, A. R. Ross, D. L. Schlagel, A. E. Clark, and M. Wun-Fogle, J. Alloys Compd. **350**, 95 (2003).

[10] R. Grössinger, R. Sato Turtelli, N. Mehmood, S. Heiss, H. Müller, and C. Bormio-Nunes, J. Magn. Magn. Mater. (to be published).

[11] A. E. Clark, K. B. Hathaway, M. Wun-Fogle, J. B. Restorff, T. A. Lograsso, V. M. Keppens, G. Petculesci, and R. A. Taylor, J. Appl. Phys. **93**, 8621 (2003).

[12] R. Wu, J. Appl. Phys. **91**, 7358 (2002).

[13] J. Cullen, P. Zhao, and M. Wuttig, J. Appl. Phys. **101**, 123922 (2007).

[14] A. Filipponi, M. Borowski, D. T. Bowron, S. Ansell, S. De Panfilis, A. Di Cicco, and J.-P. Itie, Rev. Sci. Instrum. **71**, 2422 (2000).

[15] K. H. J. Buschow, P. G. van Engen, and R. Jongebreur, J. Magn. Magn. Mater. **38**, 1 (1983).

[16] P. Scherrer, Nachr. Ges. Wiss. Goettingen, Math.-Phys. Kl. **2**, 98 (1918).

[17] P. A. Lee, P. H. Citrin, P. Eisenberger, and B. M. Kincaid, Rev. Mod. Phys. **53**, 769 (1981).

[18] E. A. Stern, M. Newville, B. Ravel, Y. Yacoby, and D. Haskel, Physica B **208-209**, 117 (1995).

[19] M. Newville, P. Livins, Y. Yacoby, J. J. Rehr, and E. A. Stern, Phys. Rev. B **47**, 14126 (1993).

[20] A. L. Ankudinov, B. Ravel, J. J. Rehr, and S. D. Conradson, Phys. Rev. B **58**, 7565 (1998).

[21] B. Ravel, J. Synchrotron Radiat. **8**, 314 (2001).

[22] M. Newville, J. Synchrotron Radiat. **8**, 322 (2001).

[23] U. Scheuer and B. Lengeler, Phys. Rev. B **44**, 9883 (1991).

[24] A. S. Nowick and B. S. Berry, *Anelastic Relaxation in Crystalline Solids* (Academic, New York, 1972).